Gravity Field of the Orientale Basin from the Gravity Recovery and Interior Laboratory Mission

Maria T. Zuber[1,*], **David E. Smith**[1], **Gregory A. Neumann**[2], **Sander Goossens**[3], **Jeffrey C. Andrews-Hanna**[4,5], **James W. Head**[6], **Walter S. Kiefer**[7], **Sami W. Asmar**[8], **Alexander S. Konopliv**[8], **Frank G. Lemoine**[2], **Isamu Matsuyama**[9], **H. Jay Melosh**[10], **Patrick J. McGovern**[7], **Francis Nimmo**[11], **Roger J. Phillips**[5], **Sean C. Solomon**[12,13], **G. Jeffrey Taylor**[14], **Michael M. Watkins**[8,15], **Mark A. Wieczorek**[16], **James G. Williams**[8], **Johanna C. Jansen**[4], **Brandon C. Johnson**[1,6], **James T. Keane**[9], **Erwan Mazarico**[2], **Katarina Miljkovi** [1,17], **Ryan S. Park**[8], **Jason M. Soderblom**[1], **Dah-Ning Yuan**[8]

[1]Department of Earth, Atmospheric and Planetary Sciences, Massachusetts Institute of Technology, Cambridge, MA 02139-4307, USA.

[2]Solar System Exploration Division, NASA Goddard Space Flight Center, Greenbelt, MD 20771, USA.

[3]Center for Research and Exploration in Space Science and Technology, University of Maryland, Baltimore County, Baltimore, MD 21250, USA.

[4]Department of Geophysics and Center for Space Resources, Colorado School of Mines, Golden, CO 80401, USA.

[5]Southwest Research Institute, Boulder, CO 80302, USA.

[6]Department of Earth, Environmental and Planetary Sciences, Brown University, Providence, RI 02912, USA

[7]Lunar and Planetary Institute, Houston, Texas 77058, USA.

[8]Jet Propulsion Laboratory, Pasadena, CA 91109, USA

[9]Lunar and Planetary Laboratory, University of Arizona, Tucson, AZ 85721-0092, USA

[10]Department of Earth, Atmospheric, and Planetary Sciences, Purdue University, West Lafayette, IN 47907, USA.

[11]Department of Earth and Planetary Sciences, University of California, Santa Cruz, Santa Cruz, California 95064, USA.

[12]Department of Terrestrial Magnetism, Carnegie Institution of Washington, Washington, DC 20015, USA.

[13]Lamont-Doherty Earth Observatory, Columbia University, Palisades, NY 10964, USA.

*To whom correspondence should be addressed: zuber@mit.edu.

Supplementary Materials
Supplementary Text
Figs. S1, S2, S3, S4, S5, S6, S7, S8
References (41–76)

[14]Hawaii Institute of Geophysics and Planetology, University of Hawaii, Honolulu, HI 96822, USA.

[15]Center for Space Research, University of Texas, Austin, TX 78712 USA.

[16]Institut de Physique du Globe de Paris, Sorbonne Paris Cité, Université Paris Diderot, 75205 Paris Cedex 13, France.

[17]Department of Applied Geology, Curtin University, Perth, WA 6845, Australia.

Abstract

The Orientale basin is the youngest and best-preserved major impact structure on the Moon. We used the Gravity Recovery and Interior Laboratory (GRAIL) spacecraft to investigate the gravitational field of Orientale at 3–5-km horizontal resolution. A volume of at least $(3.4\pm0.2)\times10^6$ km^3 of crustal material was removed and redistributed during basin formation. There is no preserved evidence of the transient crater that would reveal the basin's maximum volume, but its diameter may now be inferred to be between 320 and 460 km in diameter. The gravity resolves distinctive structures of Orientale's three rings, and suggests the presence of faults that penetrate the mantle associated with the outer two. The crustal structure of Orientale provides constraints on the formation of multi-ring basins.

Basin-scale impacts disrupted early planetary crusts and imparted substantial kinetic energy that led to fracturing, melting, vaporization, seismic shaking, ejection, and redistribution of crustal and possibly mantle material. Impact basins preserve the record of these planet-altering events, and the study of these structures elucidates the partitioning of energy and its corresponding geological and environmental effects early in planetary history. Surface signatures of impact basins on solid planets have been extensively documented (1, 2), but their subsurface structure has, to date, been poorly characterized. We present a high-resolution orbital gravity field model of the Orientale basin on the Moon as mapped by the Gravity Recovery and Interior Laboratory (GRAIL) mission (3).

Orientale, located on the western limb of the lunar nearside, is the youngest (~ 3.8-Gy old) (1, 4) large (~930-km-diameter) impact basin on the Moon. As a consequence of its good state of preservation (1, 5), with relatively few superposed large craters (6), it is often considered the standard example of a well-preserved, multi-ring basin in comparative studies of large impacts on terrestrial planetary bodies (2, 7). Because of the basin's importance, the GRAIL Extended Mission (supplementary online text) featured a low-altitude mapping campaign during the mission's Endgame phase (8), in which the dual spacecraft orbited the Moon at an average altitude of 6 km and acquired observations less than 2 km above the basin's eastern rings (Figs. S1 and S2).

To produce the highest-resolution gravity map achievable from the data and to assure that small-scale features resolved were robust, we developed two maps that used the same data but independent methodologies (9). The first is derived from a global spherical harmonic expansion of GRAIL's Ka-band (32 GHz) range-rate (KBRR) tracking data to degree and order 1200 (spatial block size = 4.5 km). The second is from a local model that implemented a short-arc analysis (10) of the tracking data and used a gravitational field model to degree and order 900 (11) as the a priori field. Local gravitational anomalies were estimated with

respect to the spherical harmonic model at the center coordinates of a set of grid points. The final model has a mixed grid resolution $0.1° \times 0.1°$ and $0.1667° \times 0.1667°$, corresponding to a maximum spatial resolution varying between 3 and 5 km. These independent analyses produced gravitational models of Orientale that are essentially indistinguishable (cf. Fig. S4). The maps are shown in Fig. 1; they resolve the shallow subsurface structure of Orientale at a spatial resolution comparable with that of many geological structures at the surface, including simple and secondary craters.

The topography of the Orientale basin (12) from the Lunar Orbiter Laser Altimeter (13) and the free-air gravity anomaly field of the region are shown in Figs. 1A and 1B. The maps show similar detail at small spatial scales because above degree and order 80 (spatial block size < 68 km) more than 98% of the lunar gravity field is attributable to topography (14). The high correlation of topography and gravity at short horizontal scales is due to the large magnitude of the gravity anomalies arising from topography relative to the weaker anomalies attributable to density anomalies in the shallow subsurface (14).

Both topography and free-air gravity anomaly resolve Orientale's Inner Depression (ID), as well as the Inner Rook ring (IRR), Outer Rook ring (ORR), and Cordillera ring (CR) (see Fig. 1). The rings, which were only partially resolved in pre-GRAIL gravitational models (15), formed in the process of cavity collapse during the modification stage of the impact event, within an hour of the initiation of basin formation (16). The mechanism for ring formation, however, has been controversial (2, 5, 17–19), in large part because of a lack of understanding of subsurface structure needed to provide constraints on impact basin formation models.

Variations in sub-surface mass are best revealed in the Bouguer gravity anomaly field (Fig. 1C), a representation of the gravitational field after the attraction of surface topography has been removed. Determination of crustal structure requires careful consideration of likely crustal and mantle composition (supplementary online text). For uniform-density crust and mantle (2550 and 3220 kg m^{-3}, respectively (20)), the Bouguer gravity anomaly can be used to map the crust-mantle boundary, and thus crustal thickness (Fig. 1D, Fig. S5). Although the assumption of uniform density is an approximation, its application to the regional crustal structure is supported by crustal density inferred from GRAIL (20) as well as from orbital remote sensing data (supplementary online text and Fig. S6). Some models for the crust invoke a mixed feldspathic layer that overlies a layer of pure anorthosite (21), but the density contrast between these rock types is small in comparison with that across the crust-mantle interface. In the mantle there is likely a pronounced seismic discontinuity at 500–600 km depth, about the scale of Orientale, marking a change in mantle composition, and hence density (22); lateral variations in this depth will contribute to the Bouguer signal. However, the density contrast is provided by a change in mafic mineralogy, which is small compared to the density change at the crust-mantle boundary. Furthermore, the signal is attenuated to the extent that only the broadest length scales of the crustal model might be affected.

A cross-section of crustal structure along the profile in Fig. 1D is shown in Fig. 2. Crust-mantle boundary profiles take into account the effect on the crustal structure of a 10-km-thick sheet of density 2650 kg m^{-3} confined to the inner depression to represent solidified

impact melt or crustal material formed by differentiation of Orientale's melt pool (9) ; in the end-member case in which the sheet is instead identical in density to feldspathic crust, the minimum crustal thickness would be only 2 km less. Consequently, the presence of a high-density sheet does not have a substantial effect on the basin's crustal structure. Fig. 1D indicates that the Orientale impact removed and redistributed a minimum of $(3.4 \pm 0.2) \times 10^6$ km^3 of material (9) from the lunar crust. Approximately one-third of the excavated material was deposited as ejecta in an annulus between the Cordillera ring and a radial distance from the basin center of one basin diameter (23), contributing to enhanced crustal thickness in this region (Fig. 1D). The high porosity (~18%) inferred in the Orientale ejecta blanket (20, 24) is similar to the porosity observed in Apollo 14 samples of the Fra Mauro Formation, which consist of ejecta from the Imbrium basin (25).

The calculation of crustal thickness does not include the presence of the mare units that are generally less than 1 km thick and irregularly distributed within the Inner Depression and ponded irregularly inside the Outer Rook and Cordillera rings (21) (low-reflectance areas in Fig. S7). The gravitational signal of the mare units is partially masked by the unknown characteristics of the impact melt sheet, and where these deposits are present, the underlying crustal thickness would be slightly greater than in the model.

Pre-GRAIL gravitational models have shown that the most distinct, well-preserved, large-scale gravitational signature associated with large lunar basins is a strong central positive free-air anomaly (26–29). These mass excesses or mascons (30) are a consequence of the thinning of the crust beneath the basin combined with mantle rebound and subsequent isostatic uplift of the central basin that was mechanically coupled to surrounding crust (31, 32). Figs. 1 and 2 show that in Orientale, the diameter of crustal thinning corresponds closely to the diameter of the Inner Depression. We therefore identify the Inner Depression as an approximation to the basin excavation cavity, i.e., the region in which the crust was thinned from its pre-impact state (21).

Of interest in impact studies is the transient crater - the cavity formed at the culmination of excavation, prior to collapse and modification. The transient crater corresponds to the maximum displaced volume, and its diameter satisfies standard impact scaling laws (33, 34), which allow many characteristics of an impact to be inferred from its size. Although there is general recognition that the transient crater should not be preserved, each of Orientale's basin rings has been variously interpreted as marking the diameter of the transient crater (2, 5, 17, 18, 35). GRAIL's improved spatial resolution and signal sensitivity shows no evidence of the transient crater, indicating that any remnant is not preserved or at least not recognizable in the gravity field. However, the transient crater diameter may now be calculated with confidence from scaling laws (36). From the 530-km diameter of the annular maximum in crustal thickness (Fig. 1D) measured from an azimuthally averaged crustal thickness profile (Fig. S5), the transient crater diameter is between 320 and 460 km, placing it between the diameters of Orientale's Inner Depression and Inner Rook ring. The transient crater thus does not correspond to a specific ring; indeed, hydrocode modeling constrained by this crustal structure model (16) indicates that rings form subsequent to the transient crater, during the collapse phase.

The transition between the basin excavation cavity and the surrounding crust is well illustrated in Fig. 2. At the outer edges of the zone of mantle uplift, the crust-mantle boundary slopes outward and downward by at least 20°–25°. The spatial correspondence of this plug of uplifted mantle with the Inner Depression is similar to the pattern seen in other multi-ring basins (37), but it is in contrast to peak-ring basins, where the zone of uplifted mantle is limited to the area within the peak ring.

The model also shows, beyond the basin depression, an annulus of thickened crust (Figs. 1D and S8D), as well as radial structure in gravity gradients (Figs. 1E and S8E) that locally correlates with observed ejecta structures (e.g., secondary crater chains) (23).

Aspects of Orientale's asymmetry in surface structure extend to the subsurface, as indicated in Figs. 1 and 2. For instance, the basin exhibits an east-west variation in regional crustal structure that predated formation of the basin.

There are also radial variations in crustal thickness, some of which are distinctly associated with Orientale's outer two basin rings. The simplest interpretation of the azimuthally averaged models is that they could correspond to displacements associated with normal faults that penetrate the crust. The crust-mantle boundary relief in Fig. 2B suggests there could be multiple faults dipping inward from the Outer Rook and Cordillera rings. The crustal thickness model also suggests the presence of other crustal faults that lack a visible surface expression. Although these faults may be listric, i.e., the dip angle may decrease with depth, a dip of 50°, indicated by hydrocode simulations (16), is consistent with prominent changes in crust-mantle boundary depth. These simulations also support crustal faulting not associated with rings.

Insight into the distinctive nature of each ring can be gained from scrutiny of Figs. 1, 2, and S8. The Inner Depression has the most axisymmetric and the largest variation in crustal thickness; a change in the sign of the gravity gradient (9) marks the depression's edge. The topography of the Inner Rook ring is morphologically similar to peak rings in small basins (16),. Individual peaks within the Inner Rook are associated with positive free-air and Bouguer anomalies embedded within an annulus of negative free-air and Bouguer anomalies. The Inner Rook also appears associated with a near-circumferentially continuous change in the sign of the gravity gradient (Fig. 1E) and a flattening in relief along the crust-mantle boundary.

The Outer Rook ring also displays well-developed topography consistent with the surface expression of a normal fault scarp (38). Ring topography has associated positive free-air anomalies embedded within the same annulus of negative free-air and Bouguer anomalies. The most negative Bouguer gravity in the region appears within the Outer Rook and may reflect a combination of thickening of the crust by ejecta and extensive fracturing in the crustal column. The Outer Rook displays a sign change in the gravity gradient and a mild shoaling of the crust-mantle boundary. The collective characteristics of the Outer Rook ring are consistent with local thinning of the crust by faulting.

The topography of the Cordillera ring deviates markedly from axisymmetry; it is less developed than the Inner and Outer Rook rings and has little expression in part of the basin's

southwestern quadrant. This asymmetric structure may be a consequence of the northeast-to-southwest-directed oblique impact that formed the basin (39) or pre-existing heterogeneity of crustal or lithospheric structure (2, 38), with a clear west-to-east gradient of decreasing crustal thickness still preserved (Fig. 1D). The topography of this ring is also consistent with the surface expression of a normal fault scarp (16). The ring is characterized by positive free-air and Bouguer anomalies, a gradient in crustal thickness, and a circumferentially discontinuous sign change in the gravity gradient. The variation of relief along the crust-mantle boundary strongly suggests fault penetration to the lower crust and possibly upper mantle. The gravitational signature could alternatively reflect contributions from magmatic intrusions along the irregularly developed ring fault, but regional seismic reflection profiles of a portion of the terrestrial Chicxulub impact structure, 20%−25% the size of Orientale, show ring faults that extend well into the lower crust (40).

Our observations, combined with the accompanying simulations (16) elucidate the planet-shaping thermal, tectonic, and geological consequences of Orientale, and by extension, other large impacts that dominated the early evolution of the Moon and other solid planets.

Supplementary Material

Refer to Web version on PubMed Central for supplementary material.

References and Notes

1. Wilhelms DE, The Geologic History of the Moon U.S. Geol. Survey Prof. Paper 1348 (US Govt. Printing Office, Washington, DC, 1987), 302 pp.

2. Spudis PD, The Geology of Multiring Impact Basins: The Moon and Other Planets. (Cambridge Univ. Press, Cambridge, England, 1993), 277 pp.

3. Zuber MT, Lehman DH, Smith DE, Hoffman TL, Asmar SW, Gravity Recovery and Interior Laboratory (GRAIL): Mapping the lunar interior from crust to core. Space Sci. Rev 178, doi: 10.1007/s11214-012-9952-7 (2013).

4. Stoffler D et al., Cratering history and lunar chronology. Rev. Mineral. Geochem 60, 519–596 (2006).

5. Head JW, Orientale multi-ringed basin interior and implications for the petrogenesis of lunar highland samples. Moon 11, 327–356 (1974).

6. Fassett CI et al., Lunar impact basins: Stratigraphy, sequence and ages from superposed impact crater populations measured from Lunar Orbiter Laser Altimeter (LOLA) data. J. Geophys. Res 117, doi: 10.1029/2011JE003951 (2012).

7. Howard KA, Wilhelms DE, Scott DH, Lunar basin formation and highland stratigraphy. Rev. Geophys. Space Phys 12, 309–327 (1974).

8. Sweetser TH, Wallace MS, Hatch SJ, Roncoli RB, Design of an Extended Mission for GRAIL, in AIAA Astrodynamics Specialist Conference. (Minneapolis, MN, 2012), 18 pp. (2012).

9. Materials and methods are available as supplementary materials on Science Online.

10. Rowlands DD, Ray RD, Chinn DS, Lemoine FG, Short-arc analysis of intersatellite tracking data in a gravity mapping mission. J. Geod 76, 307–316 (2002).

11. Lemoine FG et al., A degree-900 lunar gravity model from GRAIL primary and extended mission data. Geophys. Res. Lett 41, 3382–3389, doi: 10.1002/2014GL060027 (2014). [PubMed: 26074638]

12. Smith DE et al., Summary of the results from the Lunar Orbiter Laser Altimeter after seven years in orbit. Icarus, doi: 10.1016/j.icarus.2016.06.006 (2016).

13. Smith DE et al., The Lunar Orbiter Laser Altimeter investigation on the Lunar Reconnaissance Orbiter mission. Space Sci. Rev 150, 209–241, doi:10.1007/s11214-009-9512-y (2010).

14. Zuber MT et al., Gravity field of the Moon from the Gravity Recovery and Interior Laboratory (GRAIL) mission. Science 339, , doi: 10.1126/science.1231507 (2013).

15. Kattoum YN, Andrews-Hanna JC, Evidence for ring-faults around the Orientale basin on the Moon from gravity. Icarus 226, 694–707 (2013).

16. Johnson BC et al., The formation of the Orientale lunar multi-ring basin. Science, this issue (2016).

17. Head JW, in Impact and Explosion Cratering, Roddy DJ, Pepin RO, Merrill RB, Eds. (Pergamon Press, New York, NY, 1977), pp. 563–573.

18. Hodges CA, Wilhelms DE, Formation of lunar basin rings. Icarus 34, 294–323 (1978).

19. Head JW, Transition from complex craters to multi-ringed basins on terrestrial planetary bodies: Scale-dependent role of the expanding melt cavity and progressive interaction with the displaced zone. Geophys. Res. Lett 37, doi: 1029/2009GL041790 (2010).

20. Wieczorek MA et al., The crust of the Moon as seen by GRAIL. Science 339, doi: 10.1126/science.1231530 (2013).

21. Wieczorek MA, Phillips RJ, Lunar multiring basins and the cratering process. Icarus 139, 246–259 (1999).

22. Wieczorek MA et al., The constitution and structure of the lunar interior. Rev. Mineral. Geochem 60, 221–364 (2006).

23. Xie M, Zhu M-H, Estimates of primary ejecta and local material for the Orientale basin: Implications for the formation and ballistic sedimentation of multi-ring basins. Earth Planet. Sci. Lett 440, 71–80 (2016).

24. Besserer J et al., GRAIL gravity constraints on the vertical density structure of the lunar crust. Geophys. Res. Lett 41, doi: 10.1002/2014GL060240 (2014).

25. Kiefer WS, Macke RJ, Britt DT, Irving AJ, Consolmagno GJ, The density and porosity of lunar rocks. Geophys. Res. Lett 39, doi:10.1029/2012GL051319 (2012).

26. Zuber MT, Smith DE, Lemoine FG, Neumann GA, The shape and internal structure of the Moon from the Clementine mission. Science 266, 1839–1843 (1994). [PubMed: 17737077]

27. Neumann GA, Zuber MT, Smith DE, Lemoine FG, The lunar crust: Global signature and structure of major basins. J. Geophys. Res 101, 16,841–816,863 (1996).

28. Konopliv AS et al., Gravity field of the Moon from Lunar Prospector. Science 281, 1476–1480 (1998). [PubMed: 9727968]

29. Namiki N et al., Farside gravity field of the Moon from four-way Doppler measurements of SELENE (Kaguya). Science 323, 900–905 (2009). [PubMed: 19213911]

30. Muller PM, Sjogren WL, Mascons: Lunar mass concentrations. Science 161, 680–684 (1968). [PubMed: 17801458]

31. Andrews-Hanna JC, The origin of the non-mare mascon gravity anomalies in lunar basins. Icarus 222, 159–168, doi:10.1016/j.icarus.2012.10.031 (2013).

32. Melosh HJ et al., The origin of lunar mascon basins. Science 340, 1552–1555, doi: 10.1126/science.1235768, (2013). [PubMed: 23722426]

33. Schmidt RM, Housen KR, Some recent advances in the scaling of impact and explosion cratering. Int. Jour. Impact Eng 3, 543–560 (1987).

34. Ivanov BA, Melosh HJ, Pierazzo E, in Large Meteorite Impacts and Planetary Evolution, Gibson RL, Reimold WU, Eds. (Geol. Soc. Am, Boulder, CO, 2010), pp. 29–49.

35. Potter RWK, Kring DA, Collins GS, Kiefer WS, McGovern PJ, Numerical modeling of the formation and structure of the Orientale impact basin. J. Geophys. Res 118, 1–17 (2013).

36. Potter RWK, Kring D, Collins GS, Kiefer WS, McGovern PJ, Estimating transient crater size using the crustal annular bulge: Insights from numerical modeling of lunar basin-scale impacts. Geophys. Res. Lett 39, doi:10.1029/2012GL052981 (2012).

37. Neumann GA et al., Lunar impact basins revealed by the Gravity Recovery and Interior Laboratory measurements. Sci. Advances, 1, doi: 10.1126/sciadv.1500852 (2015).

38. Nahm A, Öhman T, Kring D, Normal faulting origin for the Cordillera and Outer Rook Rings of Orientale Basin, the Moon. J. Geophys. Res 118, 190–205 (2013).

39. McCauley JF, Orientale and Caloris. Phys. Earth Planet. Int 15, 220–250 (1977).

40. Gulick SPS et al., Geophysical characterization of the Chicxulub impact crater. Rev. Geophys. Space Phys 51, 31–52 (2013).

41. Hatch SJ, Roncoli RB, Sweetser TH, GRAIL trajectory design: Lunar orbit insertion through science in *AIAA Astrodynamics Conf.* (Toronto, CA, 2010), vol. AIAA 2010–8385, 8 pp., (2010).

42. . Beerer G, Havens GG, Operating the Dual-Orbiter GRAIL Mission to Measure the Moon's Gravity, paper presented at the SpaceOps 2012, 11–15 6 2012.

43. Konopliv AS et al., The JPL lunar gravity field to degree 660 from the GRAIL primary mission. J. Geophys. Res 118, doi: 10.1002/jgre.20097 (2013).

44. Lemoine FG et al., High-degree gravity models from GRAIL primary mission data. J. Geophys. Res 118, doi: 10.1002/jgre.20118 (2013).

45. Konopliv AS et al., JPL high resolution lunar gravity fields from the GRAIL Primary and Extended mission. Geophys. Res. Lett 41, doi: 10.1002/2013GL059066, 1452–1458 (2014).

46. Rowlands DD et al., Resolving mass flux at high spatial and temporal resolution using GRACE intersatellite measurements. Geophys. Res. Lett 32, doi: 10.1029/2004GL021908 (2005).

47. Luthcke SB et al., Monthly spherical harmonic gravity field solutions determined from GRACE inter-satellite range-rate data alons. Geophys. Res. Lett 33, doi: 10.10292/10005GL024846 (2006).

48. Tapley BD, Bettadpur S, Ries JC, Thompson PF, Watkins MM, GRACE measurements of mass variability in the Earth system. Science 305, doi: 10.1126/science.1099192 (2004).

49. Goossens S et al., High-resolution local gravity model of the south pole of the Moon from GRAIL extended mission data. Geophys. Res. Lett 41, 3367–3374 (2014). [PubMed: 26074637]

50. Heiskanen WA, Moritz H, Physical Geodesy. (W.H. Freeman, San Francisco/London, 1967), 403 pp.

51. Pavlis DE, Wimert J, McCarthy JJ, "GEODYN II System Description," vol. 1–5, (Stinger Ghaffarian Technologies, Inc., 2013).

52. Rowlands DD et al., Global mass flux solutions from GRACE: A comparison of parameter estimation strategies -- Mass concentrations versus Stokes coefficients. J. Geophys. Res 115, doi: 10.1029/2009JB006546 (2010).

53. Sabaka TJ, Rowlands DD, Lutchke SB, Boy J-B, Improving global mass flux solutions from Gravity Recover yand Climate Experiment (GRACE) through forward modeling and continuous time correlation. J. Geophys. Res 115, doi: 10.1029/2010JB007533 (2010).

54. Freed AM et al., The formation of lunar mascon basins from impact to contemporary form. J. Geophys. Res 119, 2378–2397 (2014).

55. Spudis PD, Martin DJP, Kramer GY, Geology and composition of the Orientale Basin impact melt sheet. J. Geophys. Res 119, 1–11 (2014).

56. Huang Q, Wieczorek MA, Density and porosity of the lunar crust from gravity and topography. J. Geophys. Res 117, doi:10.1029/2012JE004062 (2012).

57. Jolliff BL, Gillis JJ, Haskin L, Korotev RL, Wieczorek MA, Major lunar crustal terranes: Surface expressions and crust-mantle origins. J. Geophys. Res 105, 4197–4216 (2000).

58. Korotev RL, The great lunar hot spot and the composition and origin of the Apollo mafic ("LKFM") impact-melt breccias. J. Geophys. Res 105, 4317–4345 (2000).

59. Papike JJ, Ryder G, Shearer CK, in Planetary materials, Papike JJ, Ed. (1998), vol. 36, Rev. Mineral, 36, pp. 5–1 to 5–235 (1998).

60. Lucey PG, Blewett DT, Jolliff BJ, Lunar iron and titanium algorithms based on final processing of Clementine UVVIS data. J .Geophys. Res 105, 20,297,220,308 (2000).

61. Prettyman TH et al., Elemental composition of the lunar surface: Analysis of gamma ray spectroscopy data from Lunar Prospector. J. Geophys. Res 111, doi:10.1029/2005JR002656 (2006).

62. Crites ST, Lucey PD, Revised mineral and Mg# maps of the Moon from integrating results from the Lunar Prospector neutron and gamma-ray spectrometers with Clementine spectroscopy. Am. Mineral 100, 973–982 (2014).

63. Lucey PD, Mineral maps of the Moon. Geophys. Res. Lett 31, doi:10.1029/2003GL019406 (2004).

64. Vaughan WM, Head JW, Wilson L, Hess PC, Geology and petrology of enormous volumes of impact melt on the Moon: A case study of the Orientale basin impact melt sea. Icarus 223, 749–765 (2013).

65. Moore HJ, Hodges CA, Scott DH, Multi-ringed basins -- Illustrated by Orientale and associated features. Proc. Lunar Planet. Sci. Conf. 5th, Geochim. Cosmochim. Acta supp 5, 71–100 (1974).

66. Yamamoto S et al., Massive layer of pure anorthosite on the Moon. Geophys. Res. Lett 39, doi:10.1029/2012GL052098 (2012).

67. Cheek LC, Donaldson Hanna KL, Pieters CM, Head JW, Whitten JL, Distribution and purity of anorthosite across the Orientale basin: New perspectives from Moon Mineralogy Mapper data. J. Geophys. Res 118, 1–16 (2013).

68. Lognonné P, Gagnepain-Beyneix J, Chenet H, A new seismic model for the Moon: Implications for structure, thermal evolution and formation of the Moon. Earth Planet. Sci. Lett 211, 27–44 (2003).

69. Khan A, Mosegaard K, An inquiry into the lunar interior: A nonlinear inversion of the Apollo lunar seismic data. J. Geophys. Res 107, doi: 10.1029/2001JE001658 (2002).

70. Fassett CI, Head JWI, Smith DE, Zuber MT, Neumann GA, Thickness of proximal ejecta from the Orientale Basin from Lunar Orbiter Laser Altimeter (LOLA) data: Implications for multi-ring basin formation. Geophys. Res. Lett 38, doi:10.1029/2011GL048502 (2011).

71. Sharpton VL, Outcrops on lunar crater rims,: Implications for rim construction, mechanisms, ejecta volumes and excavation depths. J. Geophys. Res. Planets 119, doi: 10.1002/2013JE004523 (2014).

72. Andrews-Hanna JC et al., Giant dikes and the early expansion of the Moon revealed by GRAIL gravity gradiometry. Science 339, doi: 10.1126/science.1231753 (2013).

73. Andrews-Hanna JC et al., Structure and evolution of the lunar Procellarum region as revealed by GRAIL gravity data. Nature 514, 68–71, doi:10.1038/nature13697 (2014). [PubMed: 25279919]

74. Smith DE et al., Initial observations from the Lunar Orbiter Laser Altimeter (LOLA). Geophys. Res. Lett 37, doi:10.1029/2010GL043751 (2010).

75. Head JW, Weitz CM, Wilson L, Dark ring in Southwestern Orientale Basin: Origin as a single pyroclastic eruption,. J. Geophys. Res 107, 5001 (2002).

76. The GRAIL mission is supported by NASA's Discovery Program and is performed under contract to the Massachusetts Institute of Technology and the Jet Propulsion Laboratory. Topography was obtained from the Lunar Orbiter Laser Altimeter on the Lunar Reconnaissance Mission, managed by NASA's Goddard Space Flight Center. The NASA Pleiades and Center for Climate Simulation supercomputers were used to compute the gravity solutions. All data used in this study are archived in the Geosciences Node of the NASA Planetary Data System at http://geo.pds.nasa.gov/missions/grail/default.htm.
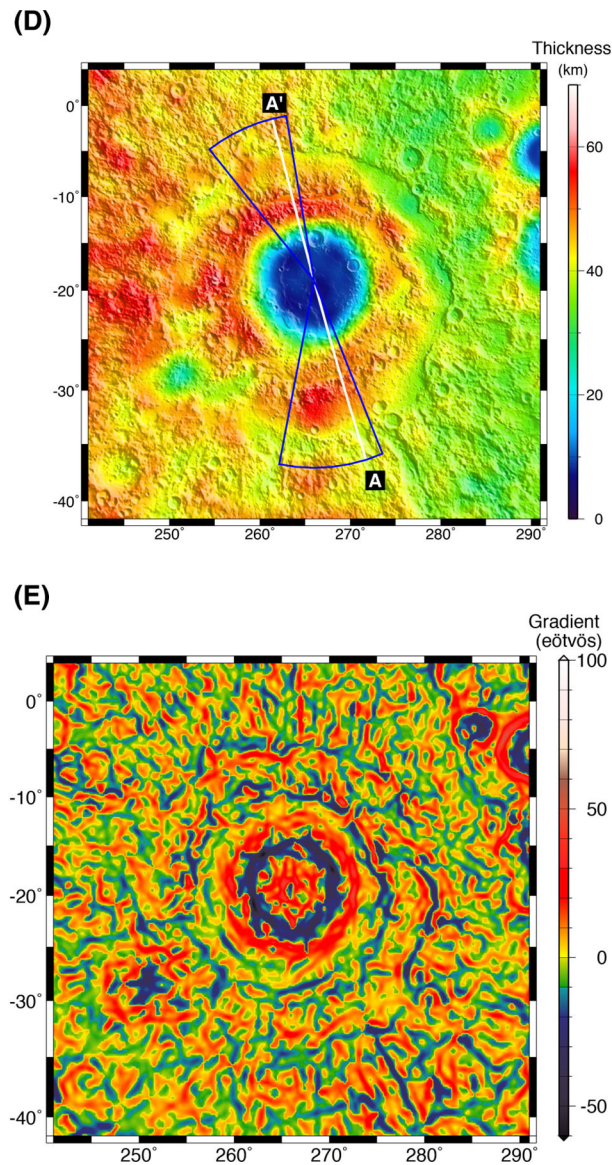
(A)

(B)

(C)

(D)

(E)
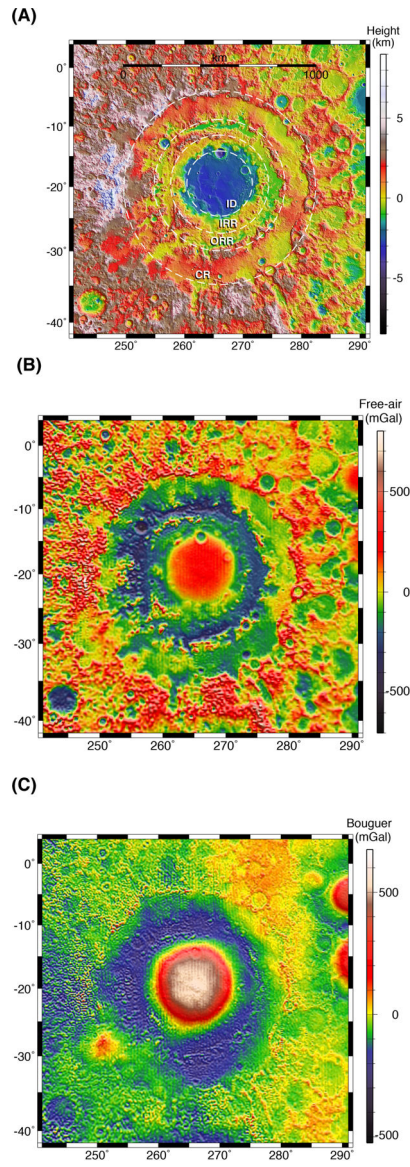
Fig. 1. High-resolution maps.

(**A**) Topography, (**B**) free-air anomaly (1mGal= 1 milliGalileo = 0^{-5} m s^{-2}), (**C**) Bouguer anomaly, (**D**) crustal thickness over shaded-relief topography, and (**E**) Bouguer gravity gradient (1 Eotovos = 10^{-4} mGal m^{-1} = 10^{-9} s^{-2}) of the Orientale basin and surroundings. Dashed lines in (**A**) from innermost to outermost correspond to the Inner Depression (ID), Inner Rook ring (IRR), Outer Rook ring (ORR), and Cordillera ring (CR). The solid white line in (**D**) shows the location of the cross-sectional profile A-A' in Fig. 2a. Blue lines show the locations of the azimuthally averaged cross-sections in Fig. 2b. Topography is updated from Lunar Observer Laser Altimeter (LOLA) (11) map LDEM_64, 0.015625° spatial resolution. To highlight short-wavelength structure, we have subtracted spherical harmonic degrees and orders less than 6 from the Bouguer gravity field. Calculation of crustal thickness and Bouguer gravity gradient are discussed in the Supplementary Online material (9).
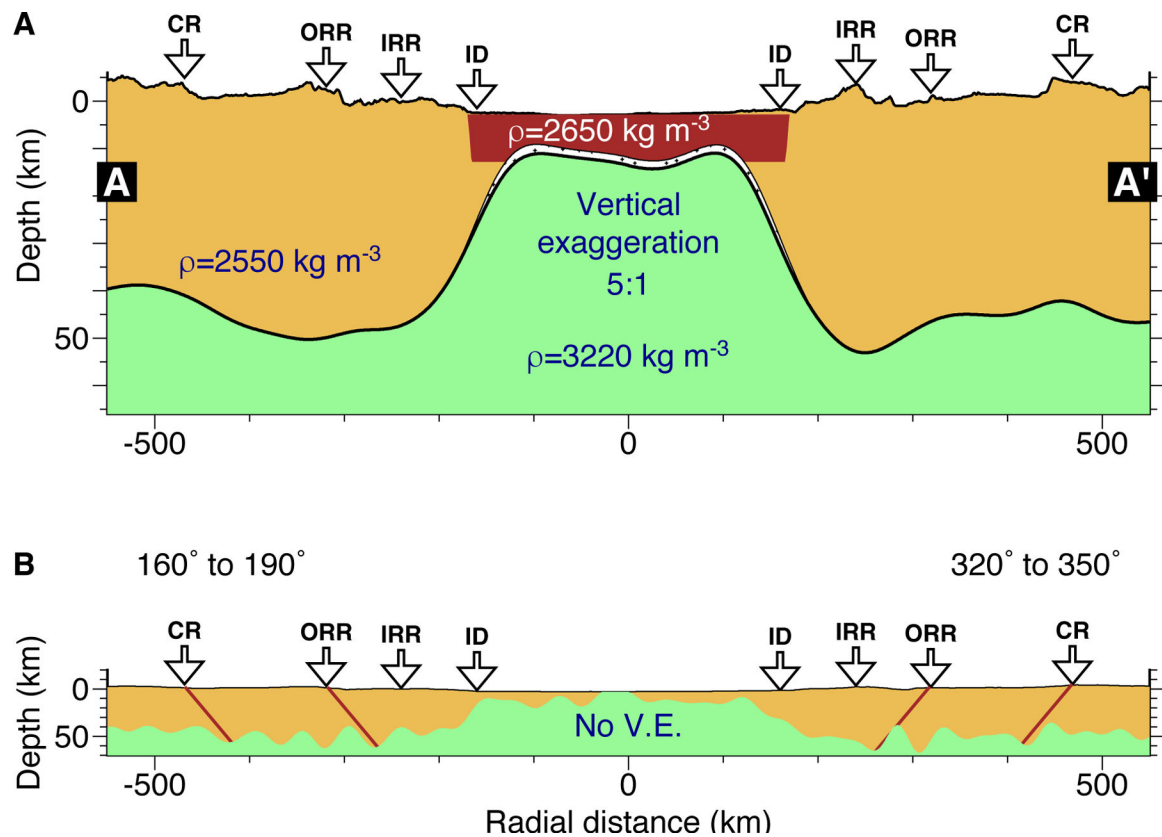
Fig. 2. Crustal cross-section.

(A) Subsurface structure of the Orientale basin along the profile shown in Fig. 1D, from southeast to northwest. Crust is shown as tan, melt sheet as red, and mantle as green. Arrows above the cross-section denote, inward to outward, Orientale's Inner Depression (ID), Inner Rook ring (IRR), Outer Rook ring (ORR), and Cordillera ring (CR). The heavy solid line indicates the base of the crust in the presence of a melt sheet that is 10 km thick, 350 km in diameter, and 2650 kg m^{-3} in density; the thin solid line indicates the base of the crust if the melt sheet density is identical to that of the crust. Vertical exaggeration (V.E.) is 5:1. **(B)** As in **(A)**, with no vertical exaggeration and 3x higher resolution filter for downward continuation (9) having higher resolution by a factor of 3, the profile is azimuthally averaged in sectors (azimuth measured clockwise from north, see Fig. 1D) to suppress noise. Red lines give the location of proposed faults dipping inward at 50° dip angle from the nominal surface positions of the ORR and CRR. Other variations in crust-mantle boundary depth suggest the presence of additional faults.